Analysis of 3D crack patterns in a free plate caused by thermal shock using FEM-bifurcation

**Nico Jesch-Weigel · Reiner Zielke ·
Martin Hofmann · Thomas Wallmersperger**

Abstract Damage to components made of brittle material due to thermal shock represents a high safety risk. Predicting the degree of damage is therefore very important to avoid catastrophic failure. An energy-based linear elastic fracture mechanics bifurcation analysis using a three-dimensional finite element model is presented here, which allows the determination of crack length and crack spacing for a defined thermal load in a free plate. It is assumed that a hierarchical crack pattern is formed due to cooling penetration. The constant growth of the ideal regular pattern of hexagons can change into a pattern with a different symmetry by slightly changing the cooling conditions. This bifurcation point is determined by the second derivative of the mechanical potential with respect to the geometry of the crack front. The very high computational effort for the second derivative is reduced by describing the three-dimensional crack front with a limited number of Fourier coefficients. A one-dimensional transient temperature field at a sufficient distance from the plate edge is assumed. For alumina, the crack length and crack spacing curves are computed for different quenching temperatures and heat transfer coefficients. The corresponding final crack lengths are also calcu-

lated as a measure of damage. Comparison with a two-dimensional model confirms the expected $1/2$ difference in crack spacing. Data from thermal shock experiments are also presented. However, due to the cracks caused by the strong cooling at the edge, these correspond to the results of the two-dimensional model.

Keywords Thermal shock · 3D crack pattern · Ceramics · Bifurcation analysis · Linear elastic fracture mechanics

N. Jesch-Weigel (✉) · M. Hofmann · T. Wallmersperger
Institut für Festkörpermechanik, TU Dresden,
George-Bähr-Straße 3c, 01069 Dresden, Germany
e-mail: Nico.Jesch-Weigel@tu-dresden.de

R. Zielke
RIF Institut für Forschung und Transfer e.V., Joseph-von-Fraunhofer Str. 20, 44227 Dortmund, Germany

List of symbols

$a(s)$	Contour of crack front
a_0	Crack length, distance between crack front and plate surface (characteristic length)
a_{end}	Final crack length
b	Half of the plate thickness (characteristic length)
C_i	Fourier coefficients
C_p	Specific heat capacity
D	Thermal diffusivity
E	Young's modulus
G	Global energy release rate
G_c	Critical energy release rate
G_{cFEM}	Energy release rate from FE analysis
$\mathbf{H}$	Hessian matrix
h	Heat transfer coefficient
h_a	Step size of the crack length for FDM

h_δ	Step size of the penetration length for FDM
$\mathbf{I}$	Identity matrix
K_I	Mode I stress intensity factor
K_{IC}	Critical mode I stress intensity factor
L	Crack spacing (characteristic length)
l_0	Fracture mechanical length (characteristic length)
l_{0FEM}	Fracture mechanical length from FE analysis
l_{0Mat}	Fracture mechanical length from given material properties
n_i	Normal vector
$\tilde{p}$	Column side width
s	Projected path variable along hexagonal crack front
T_0	Temperature of the heated plate before quenching
T_1	Temperature of the cooling liquid
$T(z, \delta), T$	Temperature field depending on location z and penetration length $\delta(t)$
t	Time
U_{el}	Elastic strain energy
u_i	Displacement, displacement vector
$\mathbf{v}$	Eigenvector
W_{fr}	Fracture energy
α	Thermal expansion coefficient
δ	Time dependent penetration length of the temperature field
δ_{ij}	Kronecker symbol
$\varepsilon_{ij}^{el}, \varepsilon_{ij}^{th}$	Strain tensor, el-elastic, th-thermal
κ	Thermal conductivity
λ	Eigenvalue
ν	Poisson's ratio
Π	Global mechanical potential
ρ	Material density
σ_{ij}	Stress tensor

Abbreviations

1D, 2D, 3D	One-, two-, three-dimensional
BEM	Boundary element method
CT	Computed tomography
FDM	Central finite difference method
FE(M)	Finite element (method)

1 Introduction

The study of thermal shocks in brittle materials and the accompanying damage in form of cracks employed by scientists for decades. Fascinating complex crack pattern formations arise during thermal shock. Beside this it is also important to know the residual strength after a thermal shock case to avoid catastrophic failure in technical systems such as gas turbines. Engineering ceramics are widely used as thermal barriers, as they can withstand very high temperatures. This application is always critical due to the relatively low fracture toughness of ceramics. It was analyzed in Kingery (1955) and Hasselman (1963, 1969) which material properties affect thermal shock damage. This was investigated experimentally by quenching alumina rods in water (Hasselman 1970). An overview of various failure phenomena and related thermal stress resistance parameters is given in Hasselman (1985).

The first investigations of 2D hierarchical parallel crack patterns and the associated analysis with a bifurcation instability criterion were carried out in Nemat-Nasser et al. (1978) and Bažant et al. (1979). Based on this criterion, the 2D crack patterns that occur when glass quartz plates are quenched in water (Bahr et al. 1986) were qualitatively investigated in Bahr et al. (1988) using the Boundary Element Method (BEM). It was found that after thermal shock the final crack length has a significant influence on the strength degradation. Nemat-Nasser et al. (1980) then published another bifurcation instability criterion which was also used in later publications (Bahr et al. 1996, 2010; Hofmann et al. 2011). In Bahr et al. (1992) another bifurcation criterion based on the mechanical potential and an eigenvalue analysis was shown. This criterion is equivalent to that of Nemat-Nasser et al. (1980). Furthermore, in Bahr et al. (1992) the correctness of the assumption of the hierarchical crack pattern, that one crack stops and another one grows, and the influence of a disturbance on it was shown. Many publications investigated crack patterns by experiments and by various simulation methods, e.g. Shao et al. (2011), Jiang et al. (2012), and Xu et al. (2016a). However, they all focus on 2D crack patterns.

In Bourdin et al. (2014), a scalar damage variable within a non-local damage model was used to simulate the growth of 3D columnar joints in thermal shocked ceramics. It was shown that this can explain the formation of imperfect polygonal patterns and their selective

coarsening during propagation, but an analysis of the 3D crack pattern geometry is still missing. 3D crack patterns of basalt columns were investigated with the Finite Element Method (FEM) in Bahr et al. (2009) by a fracture mechanic bifurcation analysis based on the local energy release rate. This research is similar to the investigated 2D cases in Bahr et al. (1988, 2009, 2010). In order to determine the 3D crack contour, an elaborate gradient method was used for the bifurcation analysis. To avoid this cumbersome iteration of the crack front, a new effective calculation method was developed based on the global energy release rate G and on a Fourier series expansion of the 3D crack front in order to simplify the bifurcation analysis. The application of this method has been demonstrated in Anderssohn et al. (2018). To enable a comparison with Bahr et al. (2009), the growth of 3D crack patterns of basalt columns was also investigated with a steady-state temperature field. The method of Anderssohn et al. (2018) can now be used to investigate the growth of other crack patterns, e.g., generated by drying or, as here, by a transient thermal shock load case for a finite length.

In the present work, we use the ideal hexagonal three column pattern from Bahr et al. (2009) and the Fourier series expansion of the 3D crack front contour from Anderssohn et al. (2018). An FE model for an infinite free plate of thickness $2b$ is built, which allows for calculating the resulting normalized crack spacing L/b and crack length a_0/b due to thermal shock. Finally, the goal of the present study is to predict the normalized final crack length a_{end}/b which is crucial for the residual strength of ceramic components that were damaged by thermal shocks.

This paper is organised as follows: Sect. 2 presents the analytical temperature field and the basic thermo-mechanical equations. In addition, the underlying model of the periodic contiuable ideal hexagonal three column pattern is described. The presentation of the theory of eigenanalysis of the global mechanical potential together with the development of the crack front geometry as a Fourier series, which was used to find the bifurcation points, concludes the section. In Sect. 3, the numerical parameters of the FE model and the central Finite Difference Method (FDM) used to determine the derivatives of the mechanical potential are explained. A convergence analysis and the effects of different numbers of Fourier series coefficients on the result are shown. Successful calculations for different temperature differences ΔT and heat transfer coeffi-

cients h were performed in Sect. 4. The influence of ΔT and h on the crack length a_0/b and the crack spacing L/b is discussed. For the validation of the 3D model, thermoshock experiments and calculations for an already existing 2D model were performed, evaluated and compared with the data of the 3D model in Sect. 5. Furthermore, a novel evaluation method based on Computed Tomography (CT) was applied to the thermo-shocked specimens in this work. Note: Similar experiments have already been performed, for example, in Shao et al. (2010) and Xu et al. (2016b). Unfortunately, no material data are given in these publications and thus cannot be used for validation. Finally, in Sect. 6, several conclusions are drawn and an outlook on possible future applications of the model presented in this paper is given.

2 Theoretical considerations

2.1 Temperature profile

First, a plate is heated to the temperature T_0 and then quenched in cooling liquid of temperature T_1. The area under consideration is the center of the plate far away from the edges. In the center the temperature field can be described by a simple 1D analytical solution, while at the edges a more complex temperature field is expected. It is assumed that the cracking process has no influence on the temperature field. This assumption is confirmed by two points: firstly, the cracks are orthogonal to the isotherms that means that they do not interfere with the heat flux. Secondly the crack opening is very small so heat transport through the air filled cracks is very small compared to the heat transport through the solid. Due to the short duration of the thermal shock process, this is a common hypothesis (Bahr et al. 1988; Li et al. 2013). Therefore, the transient temperature profile is used for an infinite plate with a thickness of $2b$ and with symmetrical boundary conditions (Tautz 1971)

$$
\begin{aligned}
T(z, \delta) = T_1 &+ \Delta T \sum_{n=1}^{\infty} \left[\frac{2 \sin(\mu_n)}{\mu_n + \sin(\mu_n) \cos(\mu_n)} \right. \\
&\left. \cos\left(\mu_n \frac{z}{b} - \mu_n\right) \exp\left(-\mu_n^2 \frac{\delta^2}{4b^2}\right) \right],
\end{aligned}
\tag{1}
$$

where $\delta = \sqrt{4Dt}$, $\mu_n = hb/\kappa \; \cot(\mu_n)$ and $\Delta T = T_0 - T_1$. Here, μ_n, $n = 1...\infty$ are the positive eigenvalues, κ the thermal conductivity, h heat transfer coefficient and D the thermal diffusivity. In Tautz (1971), the origin of the z coordinate is in the centre of the plate, whereas in the present study it is at the surface. This shift of the coordinate system is implemented in Eq. (1) by the $-\mu_n$ term in the second cosine function (see also Bahr et al. 1987, 1988).

For short times $\delta^2/4b^2 \ll 1$, (it should be noted that in the literature often τ for $\delta^2/4b^2$ is used) the number of the used eigenvalues μ_n must be high enough. Otherwise Eq. (1) is not valid (Bahr et al. 1987; Martin et al. 2019). 50 and 100 eigenvalues were calculated with the mathematic program MATLAB. For $\delta/b = 0.01$, the maximal difference of the summation term in Eq. (1) was approx $3.6 \cdot 10^{-4}$. In the simulations the smallest time is $\delta/b = 0.1$, therefore 100 eigenvalues are more than enough.

In Fig. 1 the temperature function Eq. (1) is plotted for different hb/κ and δ/b. The greater hb/κ is, the better is the heat transport between the heated plate and the cooling liquid. An increase of hb/κ leads to an increase of the temperature gradient and therefore the thermal stresses also increase. Because of that, the value of the heat transfer coefficient h is very important for the determination of the damage by the thermal shock. It should be noted that the experimental determination of h is very difficult. In Singh et al. (1981), Zhou et al. (2012), and Jiang et al. (2012) different methods were used to determine h in the case of a thermal shock of alumina in water. The results for the heat transfer coefficient h range from 10^3 Wm^{-2}K^{-1} to 10^5 Wm^{-2}K^{-1}.

2.2 Fundamental thermoelastic equations

Due to the thermal shock, the ceramic plate experiences shrinkage leading to mechanical stresses. In Takeuti and Furukawa (1981) it is shown that the ratio of $V = v_p b/D$ decides if acceleration terms have to be considered for the penetration of a temperature field. Thereby is $v_p = \sqrt{(1-\nu)E/((1+\nu)(1-2\nu)\rho)}$. The thermal diffusivity can be calculated with $D = \kappa/\rho C_p$. However, for the materials used in this work, neither D nor the specific heat capacity C_p is given, see Table 1. From Zhou et al. (2012), $D = 5.4 \cdot 10^{-6}$m^{2}s^{-1} for alumina with similar purity (99.5%) and density ($\rho =$

$3.98 \cdot 10^3$kg m^{-3}) can be taken. For the Al$_2$O$_3$ material with 99.7% purity used in the experiments, with a plate thickness of $b = 3.5 \cdot 10^{-3}$ m, $V = v_p b/D = 6.9 \cdot 10^6$ is obtained. For such large values of V, according to Takeuti and Furukawa (1981), p. 118, the ratio of dynamic and quasi-static stresses is equal to one. Thus the acceleration terms can be neglected. Volume forces are not present and the local mechanical equilibrium conditions read

$$\sigma_{ij,i} = 0 \;\; \text{and} \;\; \sigma_{ij} = \sigma_{ji} \; , \tag{2}$$

where σ_{ij} are the mechanical stresses. Eq. (2) must be fulfilled in every point of the structure. We assume an isotopic linear thermo-elastic material with linarised kinematics for which the strain ε_{ij} can separated into an elastic and a thermal part:

$$\varepsilon_{ij} = \varepsilon_{ij}^{el} + \varepsilon_{ij}^{th} = \frac{1}{2}\left(u_{i,j} + u_{j,i}\right)$$
$$= \frac{1+\nu}{E}\sigma_{ij} - \frac{\nu}{E}\sigma_{kk}\delta_{ij} + \alpha(T(z,\delta) - T_0)\delta_{ij} \; . \tag{3}$$

Here, u_i denotes the displacement, E is the Young's modulus, ν the Poisson's ratio and δ_{ij} the Kronecker symbol in the elastic strain ε_{ij}^{el}. The third term describes the thermal strain ε_{ij}^{th}. Here, α is the thermal expansion coefficient and $T(z,\delta) - T_0$ the temperature difference according to Eq. (1). T_0 is the reference temperature at which no thermal stresses are present.

For a plate having a 3D crack pattern, to which an instationary temperature field like Eq. (1) is applied, unfortunately no analytical solution of Eq. (2) is available. Therefore, the solution must be obtained numerically. In the present research, this is done by the FEM through the program Ansys. Please note that an analytical solution of the stress field which fulfills Eq. (2) for a plate without cracks is given in Timoshenko and Goodier (2017) and Parkus (1968).

2.3 Model development and boundary conditions

In experimental investigations on dried starch-water suspensions, it was found that a regular hexagonal cracking pattern causes three columns to merge into a larger one, see Fig. 2a. A similar type of column could be observed in basalt columns, which were formed by thermal contraction of solidified lava. In both cases, the
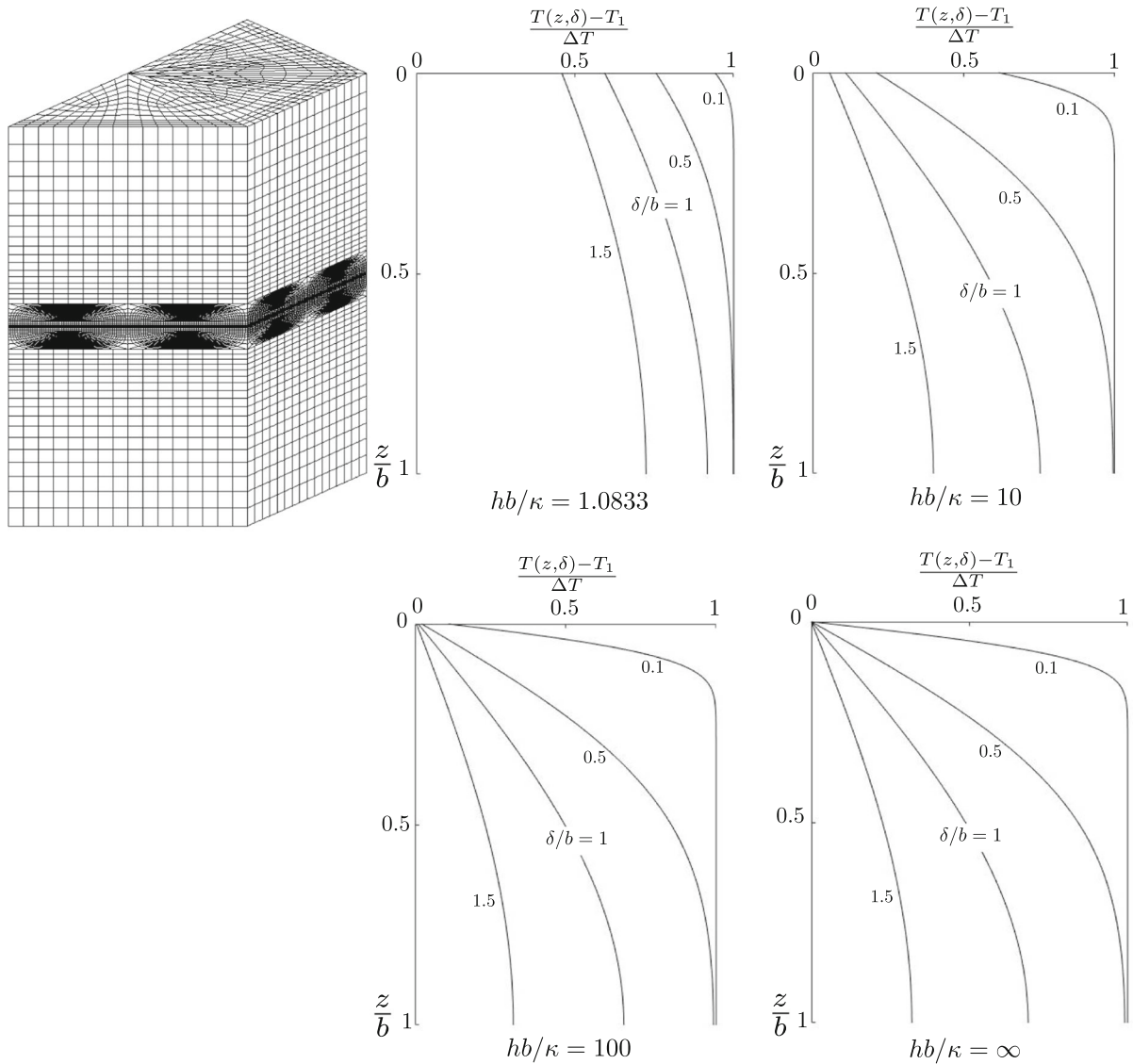
Fig. 1 Finite elemente mesh of the half hexagonal model ($a_0/b = 0.5$, $L/b = 1$) and the illustration of the temperature field (Eq. (1)) for $hb/\kappa = 1.0833$, $hb/\kappa = 10$, $hb/\kappa = 100$ and $hb/\kappa = \infty$

Table 1 Properties of AL$_2$O$_3$ ceramic plates (DOCERAM GmbH 2014; CeramTec GmbH 2015)

	ρ [kg m^{-3}]	E [GPa]	ν	K_{IC} [MPa $\sqrt{m}$]	α [K^{-1}]	κ [W m^{-1}K^{-1}]	b [m]
99.7%	$3.9 \cdot 10^3$	390	0.22	5.2	$6.95 \cdot 10^{-6}$	28	$3.5 \cdot 10^{-3}$
99.8%	$3.96 \cdot 10^3$	406	0.23	4.3	$7.5 \cdot 10^{-6}$	30	$3.25 \cdot 10^{-3}$

Fig. 2 **a** Cross-sections of crack patterns in dried starch-water suspensions demonstrating the local phenomenon of merging of three hexagonal columns into one larger hexagonal column. **b** visualisation of this process for ideal hexagonal columns (following Anderssohn et al. (2018))
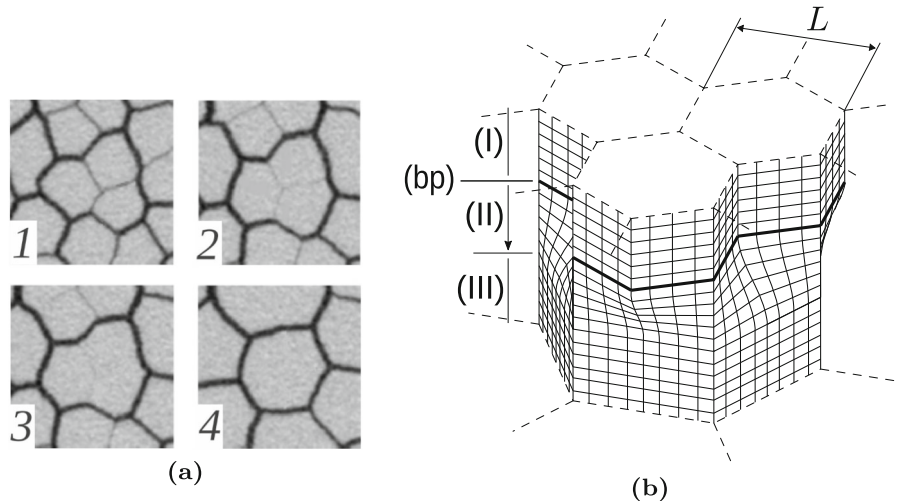
tensile stress caused by drying or cooling is the reason for the appearance of the cracks (see also Goehring et al. 2006; Goehring 2008). The process of merging three columns into one is periodically repeatable in the depth (z-direction) and also in the width of the material. This was used to form the model described below. Fig. 2b shows the idealised model with three regions. In region (I) there are three hexagonal columns of equal size with column diameter L. These columns are caused by the steady propagation of the crack front and are referred to as fundamental solution. The model then assumes that the crack stops growing at the (bp) point in the middle of the three columns. So there is another solution besides the fundamental solution. The point (bp) is hence a bifurcation point in the mathematical sense.

In region (II), the crack front between $s/\tilde{p} = 0$ and $s/\tilde{p} = 1$ in Fig. 3a stops growing. With this termination, the high symmetry of the hexagons is lost and mixed mode crack propagation with curved crack faces occurs. The three columns merge in region (III) to form a larger column with a new column diameter of $\sqrt{3}L$. It should be noted that region (II) after the bifurcation point is called the post-critical solution.

As in Anderssohn et al. (2018) and Bahr et al. (2009), we use symmetry and periodicity to reduce the computational costs. The representative volume element, used for the calculation in the case of a bifurcation, is one half of a hexagonal column (gray area in Fig. 3b). This is sufficient due to the periodic repetition. In Fig. 3b this is shown by the three points 0 in which the crack stops in the other two surrounding three hexagonal column configurations. This leads to a point symmetry with

respect to point 2 with the following coupling of the displacements in the ligament surfaces E and F of the representative volume element in Fig 3b:

$$u_z^E = u_z^F, \ u_s^E = -u_s^F \text{ and } u_n^E = -u_n^F. \tag{4}$$

Here, the index n stands for the normal direction of the ligament surfaces and s is the coordinate of the crack front. Furthermore, the stresses must be consistent at the surfaces E and F. The plate is not subjected to external kinematic constraints, so that the two surfaces G and the ligament surface at D are unloaded in the normal direction, i.e.

$$0 = \int \sigma_{ij} n_j dA \text{ and } u_i n_i = constant. \tag{5}$$

This condition was implemented by the Ansys command CE with the requirement that all FE nodes have the same displacement in the surface normal direction. The surface of the plate $z = 0$ and the crack surface are unloaded, i.e. $\sigma_{ij} n_j = 0$. The lower face, at $z = b$, is the symmetry area at which the boundary condition $u_i n_i = 0$ and $\sigma_{ij} n_j = 0$ ($i \neq j$) applies.

In the case of uniform column growth, a twelfth of the column is sufficient for the calculation since a higher symmetry is present than in the case of column merging. The ligament face B, shown in Fig. 4, is force-free in the normal direction according to Eq. (5). The faces A, C, and lower face, at $z = b$, are symmetry areas for which the boundary conditions $u_j n_j = 0$ and $\sigma_{ij} n_j = 0$ ($i \neq j$) hold. The top surface and the crack surface are free of forces $\sigma_{ij} n_j = 0$ as in the half column model.

Fig. 3 **a** Illustration of the stopping crack fronts in the postcritical solution starting from point 0 (following Bahr et al. (2009)). The grey area in **a** is redrawn in **b** (following Bahr et al. (2009)). Because of the symmetry and periodicity of the structure and process, it is sufficient to calculate only the grey area in **b**

Fig. 4 Illustration of the twelfth part of the hexagonal column (following Bahr et al. (2009))

2.4 Fracture mechanics and bifurcation

Following Anderssohn et al. (2018), we use the Fourier series

$$a(s) = a_0 + \sum_{i=1}^{j} C_i \cos\left(\frac{i\pi s}{2\tilde{p}}\right), \ 0 \le s \le 2\tilde{p} \qquad (6)$$

for the parameterization of the crack front. Here, a_0 is the crack length, j the number of cosine elements, C_i the time-invariant coefficients, $\tilde{p} = L/\sqrt{3}$ the column side width shown in Fig. 3b, and s the crack front curve variable. To ensure that the Fourier series can be used as the crack front geometry for the fundamental and also for the bifurcation solution, the product $2\tilde{p}$ is included. The function $a(s)$ is the crack length measured from the surface of the plate, as shown in Fig. 4.

For steady growth, the crack front geometries of the three-column configuration must match the opposite column. Due to the symmetry and periodicity of this configuration, $i = 4, 8, \ldots$ are the only coefficients in Eq. (6) that are nonzero. Due to the huge increase in computation time by increasing the number of coefficients and the low effect on the result (see Fig. 9), the highest Fourier coefficient C_4 is selected.

We introduce here for the case of quasi-static crack growth, the change in the global mechanical potential (see for example Kuna (2013, pp. 42–44))

$$\dot{\Pi} = \dot{U}_{el} + \dot{W}_{fr} - \dot{W}_a , \qquad (7)$$

where the elastic strain energy reads

$$U_{el} = \int \frac{1}{2} \sigma_{kl} \varepsilon_{ij}^{el} dV \qquad (8)$$

and the fracture energy

$$W_{fr} = G_C \int a(s) ds \qquad (9)$$

W_a is the external work. In Eq. (7), the dot above the symbols represents the change between two states. These states can be two different times or, as in this study, the first state is before the crack extension and the second state is after the crack extension ∂A. As there are no external forces or supports acting on the free plate,

$$\dot{W}_a = 0 . \qquad (10)$$

Furthermore, the kinetic energy equals zero. The thermal energy has no influence on the crack growth and thus the change in the thermal energy is negligible. Consequently, Eq. (7) has the character of a potential.

The integral over the crack front $a(s)$ in W_{fr} is equal to the full crack area. G_C is the critical energy release

rate of the material. Integration over the full volume of the strain energy density $\frac{1}{2}\sigma_{kl}\varepsilon_{ij}^{el}$ leads to the elastic strain energy U_{el}. The elastic strain energy U_{el} is implicitly dependent on $a(s)$. Using the Fourier series (Eq. (6)), the mechanical potential $\Pi(a(s))$, which is a functional, is thus converted into the function $\Pi(a_0, C_i)$.

As in Anderssohn et al. (2018), Hofmann et al. (2011), Bahr et al. (2009), and Bahr et al. (2010), we use characteristic lengths to scale our model and produce values with the dimension in m. Our model contains six characteristic lengths. Geometric lengths are the crack space L, half the plate thickness b, and the crack length a_0 measured from the plate surface, see Fig. 4. Furthermore, $\delta = \sqrt{4Dt}$ is the penetration depth and κ/h is the cooling length of the temperature field according to Eq. (1). From the fracture mechanics side

$$l_0 = \frac{G_c(1-\nu)}{E\alpha^2(T_0 - T_1)^2} \tag{11}$$

is the length in the 3D case. The fracture mechanics length l_0 is a value that contrasts the fracture energy per crack area $G = G_c$, necessary for crack propagation and the stored elastic energy per volume. According to Irwin (1958, p. 560), the mode I energy release rate for the 3D case can be calculated by

$$G = \frac{K_I^2(1-\nu^2)}{E}. \tag{12}$$

l_0 and κ/h are given by the mechanical and thermal material properties. The geometrical length b is given by half of the plate thickness. We consider the problem quasi-statically for a time $\delta = \sqrt{4Dt}$. For this time, a_0 and L can be calculated using the two equations for stationary crack propagation $G = G_c$ and the bifurcation criterion, which will be discussed below.

In the following we give a short overview of the bifurcation analysis considerations according to Anderssohn et al. (2018).

For stationary crack propagation, it is necessary that

$$G = G_c \tag{13}$$

is fulfilled.

The system tends to a minimum. This can be calculated by setting the first partial variation of the mechanical potential Eq. (7) to zero, i.e.

$$\dot{\Pi} = \frac{\partial \Pi}{\partial A} = \frac{\partial U_{el}}{\partial A} + \frac{\partial W_{fr}}{\partial A} = 0 \,. \tag{14}$$

Due to the mechanical potential $\Pi(a_0, C_i)$, Eq. (14) can be rewritten as

$$\frac{\partial \Pi}{\partial a_0} = \frac{\partial U_{el}}{\partial a_0} + G_c = 0 \,,$$
$$\frac{\partial \Pi}{\partial C_i} = \frac{\partial U_{el}}{\partial C_i} + G_c \int \cos\left(\frac{i\pi s}{2\tilde{p}}\right) ds = 0; \ i = [1, j], \tag{15}$$

which is the fundamental solution of the problem. This solution leads to $j + 1$ equations. G_c and l_0 are both known in Eq. (11) and if we assume that L is also given, we can use Eq. (15) to determine a_0 and C_i at a time δ. Note that changes in the pattern perpendicular to the crack growth direction are excluded in the case of the fundamental solution. This is ensured by the fact that mode I is the only stress intensity factor acting on the entire crack front.

The phenomenon of the merging of the three hexagonal columns, as described in Sect. 2.3, can be understood as a mathematical bifurcation problem. This means that there exists a second solution in addition to the fundamental one. Our goal is to find this bifurcation solution for a set of critical characteristic lengths. Starting from Eq. (15), we formed the second derivative, which leads to the Hessian matrix

$$\mathbf{H} = \Pi_{,ik} = \frac{\partial^2 \Pi}{\partial C_i \partial C_k} = \frac{\partial^2 U_{el}}{\partial C_i \partial C_k}; \ i, k = [0, j], \tag{16}$$

where $C_0 = a_0$. The eigenvalue problem

$$(\mathbf{H} - \lambda \mathbf{I})\mathbf{v} = \mathbf{0} \tag{17}$$

has a nontrivial solution when the coefficient determinant is zero

$$\det[\mathbf{H} - \lambda \mathbf{I}] = 0. \tag{18}$$

This leads to $j + 1$ eigenvalues λ_i. All eigenvalues have real values because of the symmetry of the Hessian matrix, which results in $j + 1$ real eigenvectors $\mathbf{v}_i$ computed by $(\mathbf{H} - \lambda_i \mathbf{I})\mathbf{v}_i = \mathbf{0}$.

If Eq. (18) results in positive eigenvalues, then the minimum of the mechanical potential Π (Eq. (7)) is found and the system is stable. This is the case for the fundamental solution, see Sect. 2.3. When one or more of the eigenvalues become negative, the system is unstable and bifurcation occurs. This leads to the merging of the three columns into one. The behavior after the bifurcation can be determined from the eigenvector $\mathbf{v}$ in conjunction with the fundamental solution $a(s)$

(Nguyen 1987). A set of characteristic lengths is found where the smallest eigenvalue becomes zero, i.e.

$$\lambda_{min} = 0 . \tag{19}$$

Then, the bifurcation point is reached.

The crack grows stationary as long as Eq. (13) is true. It stops growing when the condition (see also Bahr et al. 1988)

$$\left. \frac{\partial G}{\partial \delta} \right|_{a_0} = 0. \tag{20}$$

is fulfilled. This condition states that for a fixed crack length a_0 the energy release rate G does not increase even though the temperature field (the cooling) continues to penetrate. If the condition

$$\left. \frac{\partial G}{\partial \delta} \right|_{a_0} \leq 0 \tag{21}$$

is fulfilled also with the still further penetrating temperature field, it does not come again to the crack growth. Thus, the fixed crack length a_0 in Eq. (20) is the final crack length a_{end}.

3 Finite element model

In this section we will first describe the general procedure how to determine a_0/b and L/b from the FE analysis. In the following we will give more details about the used numerical methods and the influence of the number of Fourier series coefficients.

As described in Sect. 2.4 we have six characteristic lengths of which four are given. The remaining two can be determined with the condition for stationary crack growth Eq. (13) and with the condition for the occurrence of a bifurcation point Eq. (19).

For a fixed hb/κ and δ/b, for different crack lengths a_0/b and crack spacings L/b, the energy release rate G_{cFEM} is calculated according to the Eq. (15)$_1$ and the smallest eigenvalue λ_{min} is determined according to the Eqs. (16)–(18) by FE analysis. Due to the restriction to linear elastic material and small deformations, normalized material values $E = 1$, $\alpha = 1$ and a normalized temperature difference $\Delta T = 1$ can be used in the FE calculations. The dependence of ν will be discussed below. Now, by using G_{cFEM} and the normalized E, α, ΔT and a given ν, the fracture mechanical length l_{0FEM}, according to Eq. (11), can be obtained. In a further step, the searched a_0/b and L/b are now
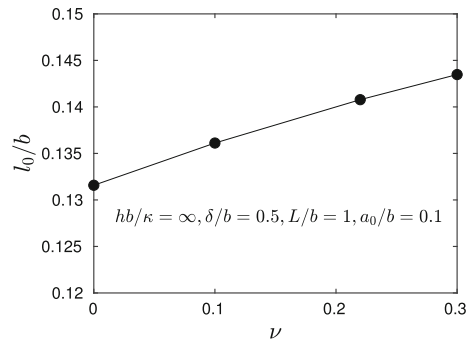
Fig. 5 Normalised fracture mechanical length l_o/b versus Poisson's ratio ν

determined. For this purpose, linear interpolation is performed between the values of λ_{min} so that Eq. (19) is fulfilled. Furthermore, l_{0Mat} is calculated from a given material, e.g. in Table 1. The fracture mechanical length l_{0FEM} is then linearly interpolated so that it matches l_{0Mat}. This corresponds to the condition for the steady-state crack growth, Eq. (13). Thus, the crack length a_0/b and crack spacing L/b were determined for a given δ/b and a given hb/κ. This process was then repeated for further δ/b and hb/κ.

Note that $\partial G/\partial \delta$ is always determined with the FE analysis. During the evaluation it can be checked whether the condition for crack stop, Eq. (20), is true. Furthermore, Eq. (11) depends on the Poission's ratio ν. In Fig. 5 the normalised fracture mechanical length l_0/b is plotted against ν. It can be seen that ν has a non-negligible influence. The dependence of ν is also given in the analytical solution of the temperature-loaded free plate in Timoshenko and Goodier (2017). Therefore, the Poisson's ratio ν of the material must be taken into account in the FE analysis.

Geometric limits result from the variation of the crack space $L/b = 0.05 \ldots 1$. The change of L causes a change of the model size and due to the meshing, the crack length is thus limited in the range of $a_0/b = 0.1 \ldots 0.9$. For some combinations of a_0/b and L/b, crack closures occur when $\delta/b < 0.5$. A more detailed investigation for the values $a_0/b < 0.1$, $L/b > 1$ and $\delta/b < 0.5$ is possible by adapting the FE mesh.

The determination of the derivatives in the fundamental solution Eq. (15), the bifurcation solution Eq. (19), and the change of the energy release rate over δ/b Eq. (20) was performed with the FDM analogous to Anderssohn et al. (2018). The central difference quo-

tient with step size h_a for crack length and h_δ for time was used for this purpose.

Isoparametric hexahedral elements with quadratic shape functions were chosen for the FE mesh. To guarantee the independence of the step size h_a in the FDM for the first and second derivatives, small step sizes are required compared to the crack spacing. This means that the strain energies must be determined as accurately as possible. Especially at the crack front, increased stresses and strains occur due to the singularity. Therefore, the crack tip was meshed with singular elements (Barsoum 1976) and a much finer discretisation was carried out in the vicinity of the crack tip (see Fig. 1). It was checked by a convergence analysis that the FE mesh is fine enough and the step sizes h_a/b and h_δ/b are sufficiently small for the FDM. Fig. 6 shows the results for the fundamental solution Eq. $(15)_1$ using the twelfth hexagonal model and Fig. 7a shows the results for λ_{min} (Eqs. (16)–(18)) using the half hexagonal model. Differences in the computation of l_0/b and λ_{min} are not recognized for the presented range of a_0/b with increasingly finer FE meshes and shorter step sizes. For the calculation of λ_{min}, the second derivative of the strain energy is needed according to Eq. (16). Thus, λ_{min} is more sensitive to numerical inaccuracies compared to l_0/b. Therefore, for λ_{min} the range in which the abscissa is cut (in which then also the bifurcation point occurs according to Eq. (19)), was shown detailed in Fig. 7b. Because of the many possible configurations for L/b, δ/b, and hb/κ, the following settings were chosen for the further analyses for certainty: 65000 nodes for the twelfth hexagonal model, 380000 nodes for the half hexagonal model and $h_a/b = 5 \cdot 10^{-4}$ for the step size of the crack length. For the choice of h_δ/b, a similar consideration was made for $\partial G/\partial \delta$ as for λ_{min} shown in Fig. 8. Again, the differences due to various step sizes h_δ/b are negligible. Based on Fig. 8b, the step size $h_\delta/b = 5 \cdot 10^{-4}$ was chosen for the further calculations.

The Hessian matrix Eq. (16) was passed to the mathematical program Matlab, where the eigenvalues λ_i were calculated.

The 1D temperature field Eq. (1) was loaded into the nodes of the 3D FE mesh using a special routine.

To determine C_4/b (according to Eq. $(15)_2$), five FEM calculations were performed with given crack length a_0/b and given crack spacing L/b using the twelfth column model (fundamental solution). From these calculations with different given values for C_4/b,
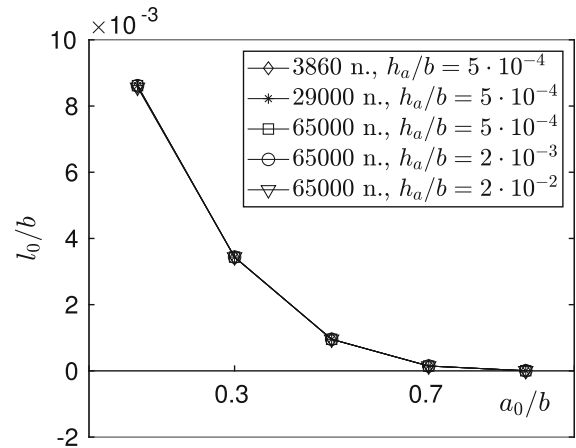
Fig. 6 Results of the convergence test calculations l_0/b according to Eq. $(15)_1$ with Eq. (11) for given $L/b = 0.5$, $\delta/b = 1$, $\nu = 0.22$ and $hb/\kappa = 1.0833$, testing three different mesh qualities (n. mean number of FE nodes) and three different step sizes h_a

five values for the elastic strain energy Eq. (8) are obtained. According to the *principle of minimum potential energy*, the correct value for C_4/b is the minimum of the least squares interpolation function. As an example, the calculated minimum and maximum values of C_4/b with the corresponding settings are given in Table 2.

The influence of the number of coefficients j in the Fourier series Eq. (6) is shown in Fig. 9. The calculations were performed for the Al_2O_3 99.8% plate (Table 1) with $h = 10^4 \text{W/m}^2\text{K}$ resulting in $hb/\kappa = 1.0833$ and $\Delta T = 800K$. The crack spacing L/b versus the crack length a_0/b is presented in Fig. 9a. In Fig. 9b, the time variation of the energy release rate $\partial G/\partial \delta$ versus the crack length a_0/b is shown. As can be seen, the difference in the results is low. This is in good agreement with the results by Anderssohn et al. (2018). For example, in Fig. 9b, where the curves cross the abscissa, the final crack length a_{end}/b is readable. The relative difference between $j = 1$ ($a_{end,C1}/b = 0.4839$) and $j = 4$ ($a_{end,C4}/b = 0.4936$) is about 2%. To save computational time, $j = 1$ (a_0 and C_1) was chosen for further calculations.

4 Crack pattern in thermo-shocked free alumina plate

It is assumed that an alumina plate is heated to a temperature T_0. Then the plate is quenched in a cooling

Table 2 Calculated minimum and maximum values of C_4/b with the corresponding settings for $hb/\kappa = 1.0833$ and $\nu = 0.23$

	δ/b	a_0/b	L/b	C_4/b
Minimal	1.1	0.1	0.05	$-2.6 \cdot 10^{-4}$
Maximal	0.45	0.9	1	$5.16 \cdot 10^{-2}$
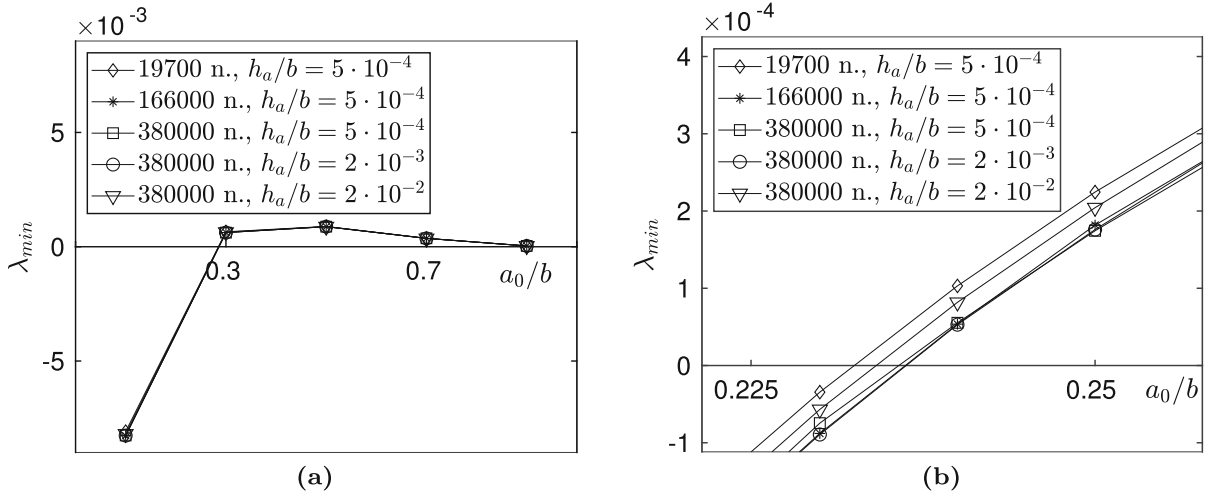
Fig. 7 **a** Results of convergence test calculations for the first eigenvalue λ_{min} according to Eq. (16)–(19), with $j = 1$ (a_0 and C_1) for given $L/b = 0.5$, $\delta/b = 1$, $\nu = 0.22$ and $hb/\kappa = 1.0833$, testing three different mesh qualities (n. mean number of FE nodes) and three different step sizes h_a, **b** detailed plot at the intersection with the abscissa
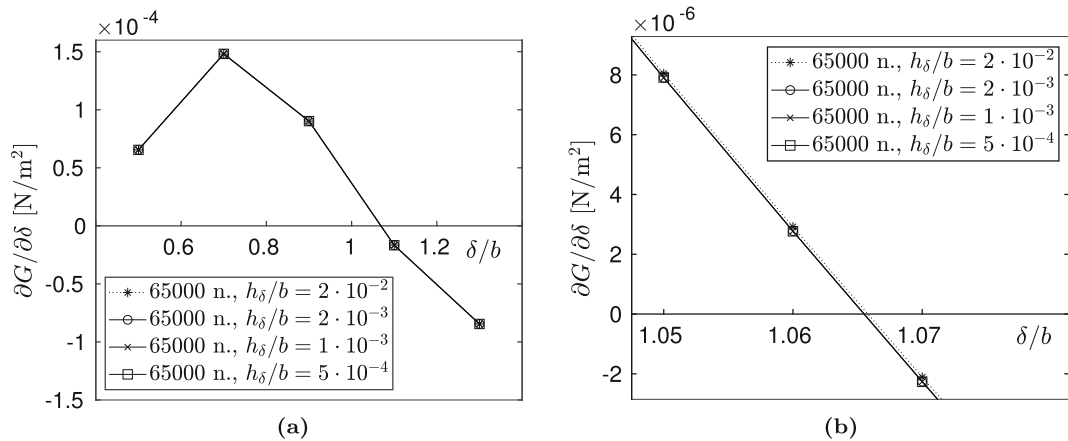
Fig. 8 **a** Results of the convergence test calculations for $\partial G/\partial \delta$ for different step sizes h_δ/b by given $L/b = 0.5$, $a_0/b = 0.5$, $\nu = 0.22$ and $hb/\kappa = 1.0833$, **b** detailed plot at the intersection with the abscissa
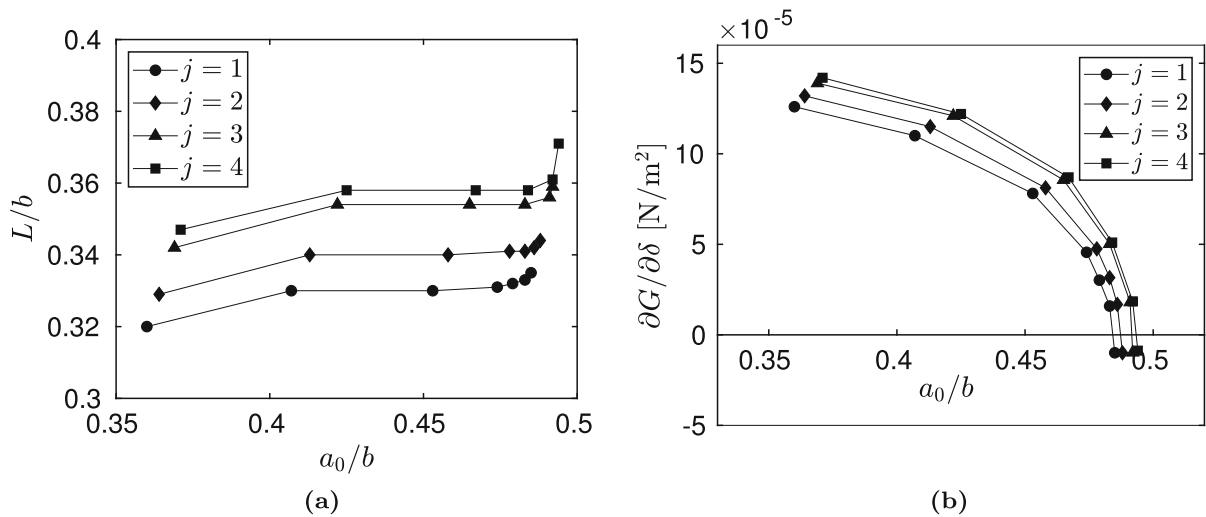
Fig. 9 Iterative calculation of the **a** crack spacing and the **b** change in the energy release rate with time for four sets of Fourier coefficients (Al$_2$O$_3$ 99.8% plate (Table 1) with $h = 10^4$ Wm^{-2}K$^{-1} \rightarrow hb/\kappa = 1.0833$ and $\Delta T = 800$ K)

liquid of constant temperature T_1. At a sufficient distance from the interface, the temperature field (Eq. (1)) holds in the plate.

Table 1 shows the material, thermal and geometrical properties of alumina plates.

Extensive simulations were performed for the Al$_2$O$_3$ 99.7% plate (Table 1). The results are illustrated in Figs. 10 and 11.

If a_{end}/b or L_{end}/b or better both are known from experiments and all parameters listed in Table 1 are also known, it is generally possible to determine the heat transfer coefficient h from diagrams like Fig. 10 between any brittle material and the cooling medium.

Here, the value $hb/\kappa = 1$ represents a kind of transition point. For $hb/\kappa < 1$, small changes of hb/κ have a very strong influence on the temperature gradient and thus on the stress. The final crack length achieved (Fig. 10a) and the final crack spacing (Fig. 10b) are very different. For $hb/\kappa > 1$, only large changes in hb/κ have a noticeable effect on a_{end}/b and L_{end}/b. If $hb/\kappa > 2$ the values of a_{end}/b and L_{end}/b very quickly approach the values of the asymptote at $hb/\kappa = \infty$. This means for the alumina plate 99.7% (Table 1) that the dependence in the final results is small for values of the heat transfer coefficient in the range $h = 16,000$ Wm^{-2}K^{-1} to $h = \infty$ Wm^{-2}K^{-1}. This could explain why in the literature, e.g. Hasselman (1970), Jiang et al. (2012), Li et al. (2013), and Xu et al.

(2016a), the heat transfer coefficient h between water and ceramics was determined to vary over a large range.

The progression of L/b over a_0/b for $hb/\kappa = 1.0833$ and $hb/\kappa = \infty$ as significant examples is shown in Fig. 11. As can be seen, L/b decreases with increasing ΔT. This could also be observed in the experiments, see Figs. 12, 13, and 14, and by Bahr et al. (1986, Fig. 2) and Xu et al. (2016b, Fig. 2) on the outside of the quenched plates. Furthermore, in Fig. 11a it can be seen that the value of the crack spacing L/b hardly changes with the growth of the crack a_0/b. This indicates that there is no merging of three columns as described in Sect. 2.3 and that the columns therefore grow in a steady course (fundamental solution). The calculated bifurcation points are not valid because the fixed point 0 in the model (Fig. 3) wants to catch up again. A postcritical analysis could show this (see Bahr et al. 2009, p. 4). However, for $hb/\kappa = \infty$ in Fig. 11b the crack space L/b is almost tripled for $\Delta T = 400$ K as well as for $\Delta T = 450$ K. For the other ΔT, L/b changes also significantly with increasing crack length. If the perturbation of the crack pattern is small enough, this will show the same trend as in Fig. 3 and the new diameter should be close to $\sqrt{3}L$. With the increase of ΔT the tensile stress increases according to Eq. (3). This leads to more cracks and thus to a decrease in the crack spacing L/b. This was also found out in 2D by thermal shock experiments with $50 \times 10 \times 1$ mm^3 thin ceramic specimens in Jiang et al. (2012, Table 1).

Consequently, the competition between short cracks increases. Short cracks have a smaller crack spacing while long cracks have a larger one.

5 Comparison with 2D model and experiments

To validate the developed model, analyses were also performed with a comparable 2D FE model. Furthermore, alumina plates were thermally quenched for different ΔT and evaluated. In Fig. 12 the results from the thermal shock experiment, the 2D and the 3D FEM bifurcation analysis are plotted. First, a brief explanation of the experiments and their evaluation is given. This is followed by a description of the 2D model with a comparison to the data from the 3D model and the experiments. At the end of this section, possible reasons why the 2D model fits the experimental data better than the 3D model are discussed.

The plates for the experiments were made of DOCE-RAM A-132 Al_2O_3 99.7% with the properties given in Table 1 with dimensions of $40 \times 40\,mm^2$. The plates were heated to $T = 550\,°C$, $750\,°C$, $950\,°C$ and quenched in boiled water of $T = 100\,°C$. The quenched temperatures were thus $\Delta T = 450\,°C$, $650\,°C$, $850\,°C$. Then the plates were treated with a contrast agent (Schilling et al. 2005) to achieve a better separation of ceramic and crack for the evaluation. Next, the plates were scanned with CT in High Aspect Ratio Tomography mode.

Through the CT scan and the contrast agent, it is possible to produce images of the surface of the sample, but also of the deep interior of the sample with the cracks highlighted, see Figs. 13 and 14.

The crack length a_0/b and the crack spacing L/b of the thermal shock experiment were measured from Fig. 14. The procedure is exemplified by Fig. 14 (e). The sectional view was loaded into the programme Engauge Digitizer version 10.10. Based on the scale line, the thickness of the sample was determined ($2b$ = 6.97 mm). Then horizontal lines were inserted from the top to the middle. These lines start and end at the outer cracks. The intersections of the lines with the cracks were counted. The crack widths are given by $L =$(width of the line)/(number of intersections -1). The associated crack length a_0 is the z-position of the line. Then the ratios L/b and a_0/b can be determined with the measured b. All information is collected in Table 3.

The 2D FE model is described in Bahr et al. (1988). For the analysis the bifurcation criterion from Nemat-Nasser et al. (1980) and Bahr et al. (1992) was used. In order to compare the results with the 3D model, the same material, thermal and geometrical settings (see Table 1 Al_2O_3 99.7%) were used in the 2D model as in the 3D model. For the 2D model, the same temperature field as in Eq. (1) was applied.

The results for the final crack length a_{end}/b with the corresponding final penetration depth of the temperature field δ_{end}/b and the final crack space L_{end}/b in the case of ideal cooling ($hb/\kappa = \infty$) are presented in Fig. 15 for the 2D and 3D FE model. The values of δ_{end}/b match quite well. The achieved values for a_{end}/b are slightly larger in the 2D FE model than in the 3D FE model. The difference for L_{end}/b is slightly larger. A factor of 2 or less between the results of the 2D FE model and those of the 3D FE model agrees well with the findings in Bahr et al. (2009). This kind of difference in a_{end}/b and L_{end}/b was also found out in the experiments by Shao et al. (2010). In our investigations, similar results were obtained for other values of hb/κ, as shown in Fig. 12.

As shown in Fig. 12, the results of the 2D analysis between $hb/\kappa = 0.5416$ and $hb/\kappa = 1.0833$ agree well with the measured values of the samples. Thus, a heat transfer coefficient between $h = 4.3 \cdot 10^3\,Wm^{-2}K^{-1}$ and $h = 8.7 \cdot 10^3\,Wm^{-2}K^{-1}$ can be determined. This is slightly lower than the measured h in Zhou et al. (2012). This is due to the fact that nucleate boiling occurs at low sample temperatures due to the lower water temperature in Zhou et al. (2012) of 20 °C, thus increasing the heat transfer coefficient. Quenching in boiling water favours the formation of a vapour film, which decreases the heat transfer coefficient (Singh et al. 1981).

It is the question of why the 2D bifurcation analysis seems to predict the crack width L/b better than the 3D one. Here are two possible explanations.

First, due to the fine grain of the material, the cracks can close again after unloading. Thus, it is possible that the contrast agent does not reach every crack and thus the cracks or their lengths are partially poorly detectable. For more details see Zielke et al. (2021).

Second, the 2D and 3D models do not predict cracks going through the entire body, see Fig. 14. In Fig. 13, especially in Fig. 13b, e, h, it can be seen that the cracks start from the edge and go into the whole body. It can be assumed that there is a surplus of energy at the edge
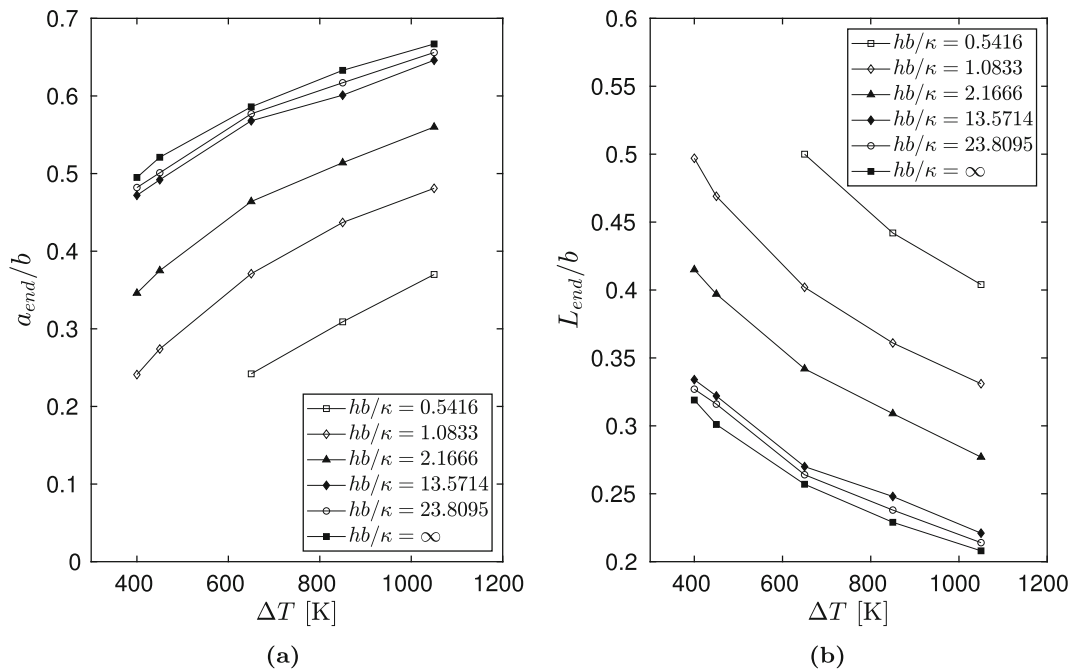
Fig. 10 **a** Normalised final crack length a_{end}/b and **b** normalised final crack spacing L_{end}/b for the alumina plate 99.7% (Table 1) for different values of hb/κ and the quenching temperatures ΔT of 400 K, 450 K, 650 K, 850 K and 1050 K
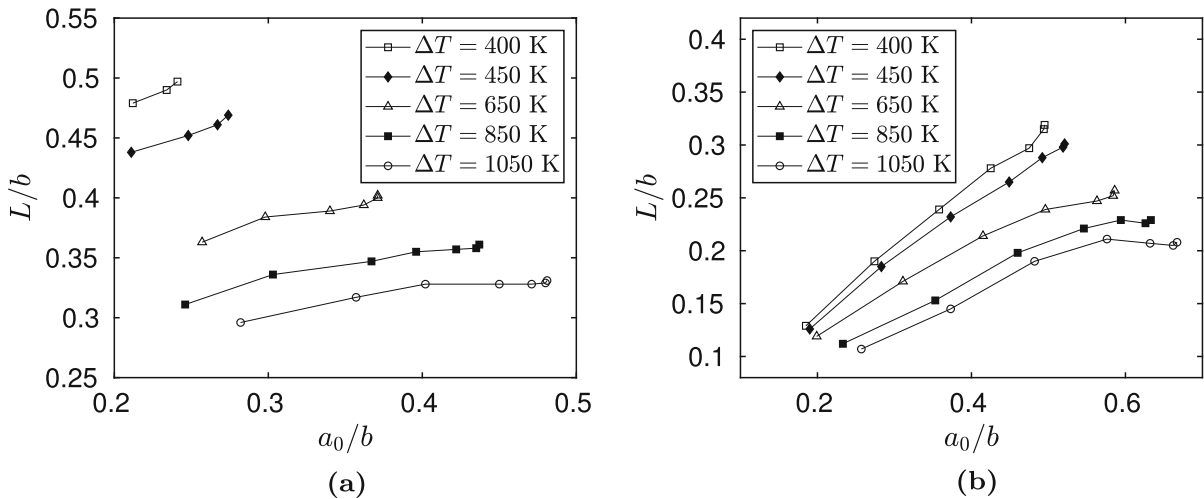

Fig. 11 Normalised crack space L/b versus normalised crack length a_0/b (to crack stop) for **a** $hb/\kappa = 1.0833$ and **b** $hb/\kappa = \infty$ for the material parameters of alumina plate 99.7% (Table 1)

due to the high temperature gradient. This causes the cracks to grow unstably into the body. The fact that the cracks also branch out is an indication of this (Kanninen and Popelar 1985, pp. 205–207). These cracks relieve the body and convert the 3D stress state in a 2D stress state.

Thus, there is no longer a closed plate when the cooling penetrates further from the surface. The penetrating cracks have cut the plate into many small slices. As has been shown by Shao et al. (2010, Figs. 3e and f), when comparing a whole plate and stacked individual plates at high temperature differences ΔT, the crack pattern

on the cooled surface looks similar. So, even for the stacked individual plates, the crack pattern is not invariant in the x- or y-direction (see also Bahr et al. 1986). However, between the interior surfaces of the stacked single plates and the cut surfaces at the whole plates, the patterns differ. Thus, more cracks are found in the whole plates, and thus a shorter crack spacing L/b, than in the interior surfaces of the stacked individual plates. This is not addressed in Shao et al. (2010). Only the fact that crack branching occurs in the stacked single plates and not in the whole plate is explained by a different stress field caused by edge effects in the stacked single plates.

One reason or a combination of both reasons may explain why the 2D bifurcation analysis fits well with the measured data from the experiments.

Nevertheless, in the following aspect the data from the 3D model, as well as the 2D model, match the experiments. Both models predict that the crack spacing will change only slightly. This means that the cracks grow stable and do not recede. This agrees well with the measured data shown in Fig. 12, although it should be noted that the increase in experimental data in L/b is due to the cracks penetrating from the edge.

6 Conclusion and future work

The model developed by Bahr et al. (2009) was applied and adapted to predict the complex growth of the hierarchical 3D crack pattern of a brittle plate under thermal shock conditions without external constraints. This model is based on the assumption that the cracks form ideal hexagonal columns and that in this idealised crack pattern, the merging of three columns into a larger column is the mechanism for increasing the crack spacing. For cooling penetration, it was assumed that a 1D stationary temperature field (Eq. (1)) exists far enough away from the edges. Based on these assumptions, a 3D FEM bifurcation analysis with the Fourier expansion of the crack front (Anderssohn et al. 2018) was performed. Besides the different type of temperature field, the following differences and extensions are present in the model used in this work compared to Bahr et al. (2009) and Anderssohn et al. (2018).

The model no longer has infinite dimensions in the z-direction but the finite thickness b. The temporal penetration of the symmetrical temperature field Eq. (1), the associated reduction of the temperature gradient

and thus the reduction of the mechanical stress, leads to crack arrest and thus to a final crack length a_{end}. The final crack length was determined by evaluating the change in the energy release rate as a function of time (Eq. (20)). a_{end} is the measure of the damage to the structure and can be used later for a residual strength analysis. Because the plate can contract without hindrance, freedom from forces in the lateral direction of the model is required.

Through a convergence study, which includes the optimisation of the FE mesh and the influence of the FDM step size, the computational effort could be reduced. Furthermore, it was shown that the results converge rapidly for an increasing number of Fourier coefficients. To reduce the computational effort even further, the different calculations were carried out with only one Fourier coefficient ($j = 1$).

Due to the linear nature of the problem and the use of the characteristic lengths, describing the material and the thermal load, it was effectively possible to determine the evolution of the crack spacing L/b over the crack length a_0/b by a parametric analysis.

The 3D model was verified by a comparison with an existing 2D model by Bahr et al. (1988). As in Bahr et al. (2009), the expected difference between 2D and 3D FE model in L/b was smaller than a factor of 2. Due to the intense cooling at the edge of the specimens and the associated formation of cracks through the whole specimen, a validation of the 3D model by experimental data was unfortunately not possible. In further research, additional experimental investigations are planned in which the specimen will be isolated at the edge. It should be noted that due to the evaluation by CT scan, the dimensions of the specimens are limited and specimens with larger dimensions cannot be simply used.

Further investigations with the presented 3D model are possible. For example, by modifying the FE mesh towards very short cracks, the critical temperature difference ΔT_c for thermal shock could be analysed at which no crack growth occurs. It should be noted that a good knowledge of the mechanical and thermal material data is important for an accurate analysis. Conversely, it is possible to determine the critical stress intensity factor K_{IC} and the heat transfer coefficient h using 3D FEM bifurcation analysis. Both values are difficult to determine using other methods. For this, the curves of a_0/b and L/b must be known from thermal shock experiments.

Fig. 12 Comparison of the normalised crack space L/b over the normalised crack length a_0/b (up to the crack stop) from the 2D and 3D FEM bifurcation analysis and the measured data of the specimen (with a resolution error of 1.4% according to the manufacturer's data of the CT device). **a**: $\Delta T = 450\ K$, no crack growth occurs in the 3D model for $hb/\kappa = 0.5416$, experimental data 1 are from Fig. 14a upper half measured, experimental data 2 are from Fig. 14b lower half measured **b**: $\Delta T = 650\ K$, experimental data 1 are from Fig. 14c lower half measured, experimental data 2 are from Fig. 14d lower half measured **c**: $\Delta T = 850\ K$, experimental data 1 are from Fig. 14e upper half measured, experimental data 2 are from Fig. 14f lower half measured

(a)

(b)

(c)
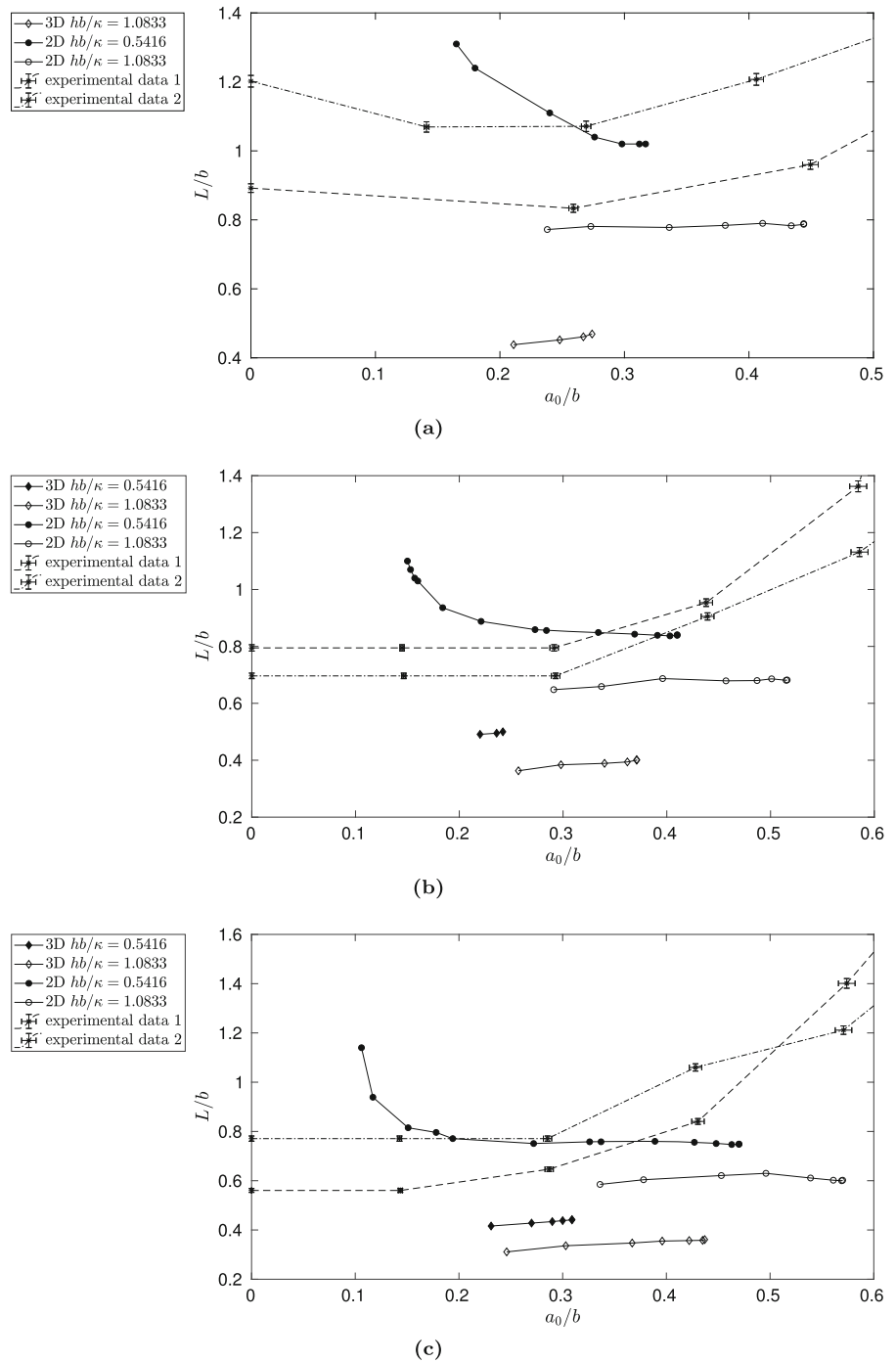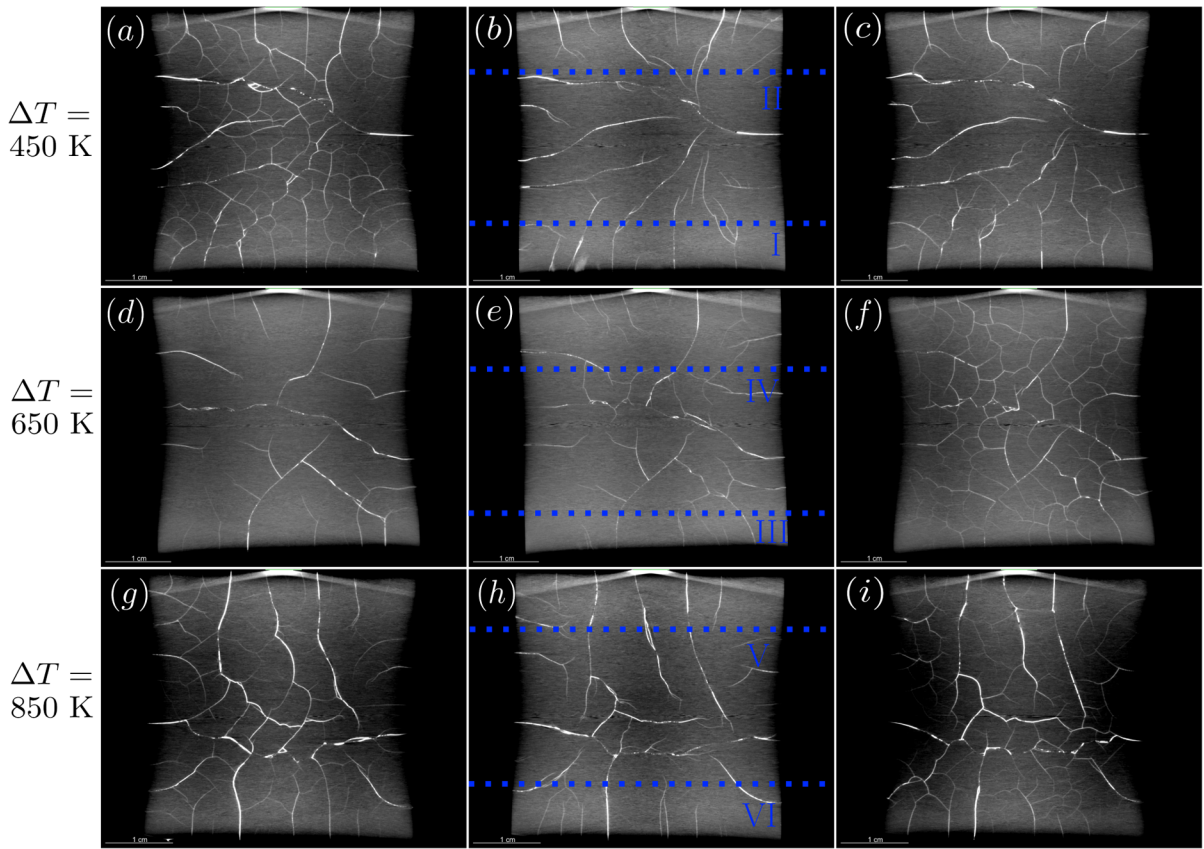
Fig. 13 Thermal shock crack patterns in Al$_2$O$_3$ 99.7% ceramic plates quenched at ΔT of **a**, **b**, **c** 450 K; **d**, **e**, **f** 650 K and **g**, **h**, **i** 850 K, whereby **a**, **d**, **g** are images of the cooled surface; **c**, **f**, **i** images from the the opposite cooled surface and **b**, **e**, **h** images from the centre of the specimen at $z = 3.5$ mm; additionally, in **b**, **e**, **h** the positions of the cross-sectional views of Fig. 14 are shown with blue dotted lines, where in Fig. 14 **a** is I, **b** is II, **c** is III, **d** is IV, **e** is V and **f** is VI
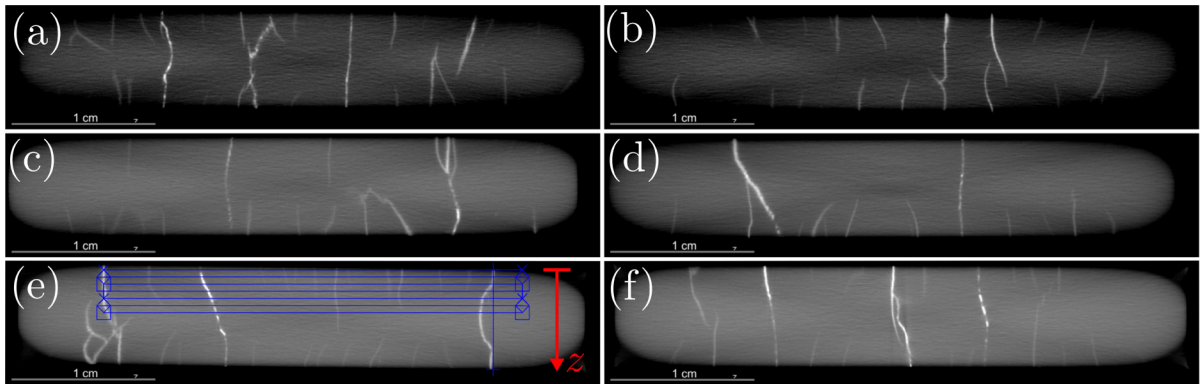
Fig. 14 Cross-sectional view of thermal shock crack patterns in Al$_2$O$_3$ 99.7% ceramic plates quenched at ΔT of **a**, **b** 450 K; **c**, **d** 650 K and **e**, **f** 850 K; the position of the cross sections are shown in Fig. 13 **b**, **e**, **h**

Table 3 Evaluation of the cross-sectional view of Fig. 14 (e) upper half

Line number	Intersections	z (mm)	Line width (mm)	L (mm)	a_0 (mm)	L/b	a_0/b
1	16	0	29.29	1.95	0	0.56	0
2	16	0.5	29.29	1.95	0.5	0.56	0.14
3	14	1	29.29	2.25	1	0.65	0.28
4	11	1.5	29.29	2.93	1.5	0.84	0.43
5	7	2	29.29	4.88	2	1.4	0.57
6	5	2.5	29.29	7.32	2.5	2.1	0.71
7	4	3	29.29	9.76	3	2.8	0.86
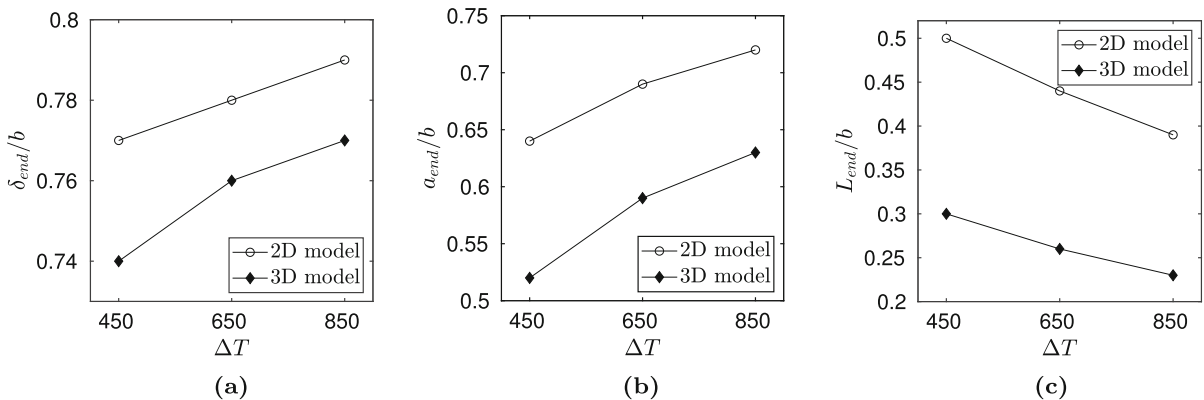
Fig. 15 Comparison of the numerically obtained results in the crack stop condition (Eq. (20)) for $hb/\kappa = \infty$ with the 2D and 3D FE model

Declarations

References

Anderssohn R, Hofmann M, Bahr HA (2018) FEM-bifurcation analysis for 3D crack patterns. Eng Fract Mech 202:363–374. https://doi.org/10.1016/j.engfracmech.2018.07.040

Bahr HA, Fischer G, Weiss HJ (1986) Thermal-shock crack patterns explained by single and multiple crack propagation. J Mater Sci 21:2716–2720. https://doi.org/10.1007/BF00551478

Bahr HA, Balke H, Kuna M, Liesk H (1987) Fracture analysis of a single edge cracked strip under thermal shock. Theor Appl Fract Mech 8:33–39. https://doi.org/10.1016/0167-8442(87)90016-4

Bahr HA, Weiss HJ, Maschke HG, Meissner F (1988) Multiple crack-propagation in a strip caused by thermal-shock. Theor Appl Fract Mech 10:219–226. https://doi.org/10.1016/0167-8442(88)90014-6

Bahr HA, Bahr U, Petzold A (1992) 1-d deterministic crack pattern formation as a growth process with restrictions. Europhys Lett 19:485–490. https://doi.org/10.1209/0295-5075/19/6/008

Bahr HA, Bahr U, Gerbatsch A, Pflugbeil I, Vojta A, Weiss HJ (1996) Fracture mechanical analysis of morphological transitions in thermal shock cracking. In: Fracture mechanics of ceramics, vol. 11 : R-Curve behavior, toughness determination, and thermal shock

Bahr HA, Hofmann M, Weiss HJ, Bahr U, Fischer G, Balke H (2009) Diameter of basalt columns derived from fracture mechanics bifurcation analysis. Phys Rev E. https://doi.org/10.1103/PhysRevE.79.056103

Bahr HA, Weiss HJ, Bahr U, Hofmann M, Fischer G, Lampenscherf S, Balke H (2010) Scaling behavior of thermal shock crack patterns and tunneling cracks driven by cooling or drying. J Mech Phys Solids 58:1411–1421. https://doi.org/10.1016/j.jmps.2010.05.005

Barsoum RS (1976) On the use of isoparametric finite elements in linear fracture mechanics. Int J Numer Methods Eng 10:25–37

Bažant Z, Ohtsubo H, Aoh K (1979) Stability and post-critical growth of a system of cooling or shrinkage cracks. Int J Fract 15:443–456. https://doi.org/10.1007/BF00023331

Bourdin B, Marigo JJ, Maurini C, Sicsic P (2014) Morphogenesis and propagation of complex cracks induced by thermal shocks. Phys Rev Lett. https://doi.org/10.1103/PhysRevLett.112.014301

CeramTec GmbH (2015) https://www.ceramtec-group.com/fileadmin/user_upload/Corporate/11_Downloads/3880_Prosp_Keram_Werkstoffe_DE-EN_Montage_web.pdf

DOCERAM GmbH (2014) https://www.moeschter-group.com/de/werkstoffe/aluminiumoxid

Goehring LAZ (2008) On the scaling and ordering of columnar joints. University of Toronto

Goehring L, Morris SW, Lin Z (2006) Experimental investigation of the scaling of columnar joints. Phys Rev E. https://doi.org/10.1103/PhysRevE.74.036115

Hasselman DPH (1963) Elastic energy at fracture and surface energy as design criteria for thermal shock. J Am Ceram Soc 46:535–540. https://doi.org/10.1111/j.1151-2916.1963.tb14605.x

Hasselman DPH (1969) Unified theory of thermal shock fracture initiation and crack propagation in brittle ceramics. J Am Ceram Soc 52:600–604. https://doi.org/10.1111/j.1151-2916.1969.tb15848.x

Hasselman DPH (1970) Strength behavior of polycrystalline alumina subjected to thermal shock. J Am Ceram Soc 53:490–495. https://doi.org/10.1111/j.1151-2916.1970.tb15997.x

Hasselman DPH (1985) Thermal stress resistance of engineering ceramics. Mater Sci Eng 71:251–264. https://doi.org/10.1016/0025-5416(85)90235-6

Hofmann M, Bahr HA, Weiss HJ, Bahr U, Balke H (2011) Spacing of crack patterns driven by steady-state cooling or drying and influenced by a solidification boundary. Phys Rev E. https://doi.org/10.1103/PhysRevE.83.036104

Irwin GR (1958) Flügge, S.: Handbuch der Physik. Band 6, Springer Verlag, Berlin,, chap Fracture, pp 551–590

Jiang C, Wu X, Li J, Song F, Shao Y, Xu X, Yan P (2012) A study of the mechanism of formation and numerical simulations of crack patterns in ceramics subjected to thermal

shock. Acta Mater 60:4540–4550. https://doi.org/10.1016/j.actamat.2012.05.020

Kanninen MF, Popelar CH (1985) Advanced fracture mechanics. Oxford University Press, New York/Clarendon, Oxford

Kingery WD (1955) Factors affecting thermal stress resistance of ceramic materials. J Am Ceram Soc 38:3–15. https://doi.org/10.1111/j.1151-2916.1955.tb14545.x

Kuna M (2013) Finite elements in fracture mechanics, theory—numerics—applications, 1st edn. Springer, Dordrecht. https://doi.org/10.1007/978-94-007-6680-8

Li J, Song F, Jiang C (2013) Direct numerical simulations on crack formation in ceramic materials under thermal shock by using a non-local fracture model. J Eur Ceram Soc 33:2677–2687. https://doi.org/10.1016/j.jeurceramsoc.2013.04.012

Martin H, Wetzel T, Dietrich B (2019) VDI-Wärmeatlas Fachlicher Träger VDI-Gesellschaft Verfahrenstechnik und Chemieingenieurwesen, 12th edn, Springer Vieweg, Berlin, chap E2 Wärmeleitung - instationär, pp 729–755

Nemat-Nasser S, Keer LM, Patihar KS (1978) Unstable growth of thermally induced interacting cracks in brittle solids. Int J Solids Struct 14:409–430. https://doi.org/10.1016/0020-7683(78)90007-0

Nemat-Nasser S, Sumi Y, Keer LM (1980) Unstable growth of tension cracks in brittle solids: stable and unstable bifurcations, snap-through, and imperfection sensitivity. Int J Solids Struct 16:1017–1035. https://doi.org/10.1016/0020-7683(80)90102-X

Nguyen Q (1987) Bifurcation and post-bifurcation analysis in plasticity and brittle fracture. J Mech Phys Solids 35:303–324. https://doi.org/10.1016/0022-5096(87)90010-X

Parkus H (1968) Thermoelasticity. Blaisdell Publishing Company, Waltham, Massachusetts

Schilling PJ, Karedla B, Tatiparthi AK, Verges MA, Herrington PD (2005) X-ray computed microtomography of internal damage in fiber reinforced polymer matrix composites. Compos Sci Technol 65:2071–2078. https://doi.org/10.1016/j.compscitech.2005.05.014

Shao Y, Xu X, Meng S, Bai G, Jiang C, Song F (2010) Crack patterns in ceramic plates after quenching. J Am Ceram Soc 93:3006–3008

Shao Y, Zhang Y, Xu X, Zhou Z, Li W, Liu B (2011) Effect of crack pattern on the residual strength of ceramics after quenching. J Am Ceram Soc 94:2804–2807. https://doi.org/10.1111/j.1551-2916.2011.04728.x

Singh JP, Tree Y, Hasselman DPH (1981) Effect of bath and specimen temperature on the thermal stress resistance of brittle ceramics subjected to thermal quenching. J Mater Sci 16:2109–2118. https://doi.org/10.1007/BF00542371

Takeuti Y, Furukawa T (1981) Some considerations on thermal shock problems in a plate. J Appl Mech 48:113–118. https://doi.org/10.1115/1.3157552

Tautz H (1971) Wärmeleitung und Temperaturausgleich. Akademie-Verlag, Berlin, Die mathematische Behandlung instationärer Wärmeleitungsprobleme mit Hilfe von Laplace-Transformationen

Timoshenko SP, Goodier JN (2017) Theory of elasticity, 3rd edn. McGraw-Hill, New York

Xu XH, Sheng SL, Tian C, Yuan WJ (2016) A comparative analysis of reticular crack on ceramic plate driven by ther-

mal shock. Sci China Phys Chem. https://doi.org/10.1007/s11433-016-0098-2

Xu X, Lin Z, Sheng S, Yuan W (2016) Evolution mechanisms of thermal shock cracks in ceramic sheet. J Appl Mech-T ASME 10(1115/1):4033175

Zhou ZL, Song F, Shao YF, Meng SH, Jiang CP, Li J (2012) Characteristics of the surface heat transfer coefficient for Al2O3 ceramic in water quench. J Eur Ceram Soc 32:3029–3034. https://doi.org/10.1016/j.jeurceramsoc.2012.04.027

Zielke R, Tillmann W, Fischoeder M, Ambaum M (2021) Einsatz von röntgenografischen Verfahren zur hochauflösenden Analyse von Rissmustern. https://www.ndt.net/search/docs.php3?id=26260